High pressure enhanced magnetic ordering and magnetostructural coupling in the geometrically frustrated spinel Mn$_3$O$_4$

D. P. Kozlenko,[1,*] N. T. Dang [ORCID],[2,3,†] S. E. Kichanov,[1] L. T. P. Thao [ORCID],[4,5,‡] A. V. Rutkaukas,[1] E. V. Lukin [ORCID],[1] B. N. Savenko,[1] N. Tran [ORCID],[2,3] D. T. Khan [ORCID],[5] L. V. Truong-Son [ORCID],[5] L. H. Khiem,[6,7] B. W. Lee [ORCID],[8] T. L. Phan,[8] N. L. Phan [ORCID],[9] N. Truong-Tho [ORCID],[4] N. N. Hieu [ORCID],[2,3] T. A. Tran [ORCID],[10,§] and M. H. Phan [ORCID][11,‖]

[1]*Frank Laboratory of Neutron Physics, Joint Institute for Nuclear Research, 141980 Dubna, Russia*
[2]*Institute of Research and Development, Duy Tan University, 550000 Danang, Viet Nam*
[3]*Faculty of Environmental and Natural Sciences, Duy Tan University, 550000 Danang, Viet Nam*
[4]*Faculty of Electronics, Electrical Engineering and Material Technology, University of Sciences, Hue University, 530000 Hue, Vietnam*
[5]*University of Science and Education, The University of Danang, 550000 Danang, Vietnam*
[6]*Institute of Physics, Vietnam Academy of Science and Technology, 100000 Hanoi, Vietnam*
[7]*Graduate University of Science and Technology, Vietnam Academy of Science and Technology, 100000 Hanoi, Vietnam*
[8]*Department of Physics and Oxide Research Center, Hankuk University of Foreign Studies, Yongin 449–791, South Korea*
[9]*Department of Physics, Ho Chi Minh City University of Education, 700000 Ho Chi Minh, Vietnam*
[10]*Ho Chi Minh City University of Technology and Education, 700000 Ho Chi Minh, Vietnam*
[11]*Department of Physics, University of South Florida, Tampa, Florida 33620, USA*

Mn$_3$O$_4$ represents a model system for probing geometrically frustrated magnetism, and studying the magnetic behavior of the material under high pressure could yield new insights into the magnetostructural coupling and structurally driven magnetic ordering transitions that are otherwise not observable at ambient pressure. We report here a systematic study of the crystal and magnetic structures of Mn$_3$O$_4$ at high pressure up to 37 and 20 GPa using x-ray and neutron powder diffraction techniques, respectively. We find that upon compression, the crystal structure transforms from the initial tetragonal hausmannite phase of $I4_1/amd$ symmetry into the orthorhombic CaMn$_2$O$_4$-type ($Pbcm$ symmetry) phase via the intermediate orthorhombic CaTi$_2$O$_4$-type ($Bbmm$ symmetry) phase. In the tetragonal phase, the application of pressure, $P > 2$ GPa, leads to the suppression of low-temperature incommensurate and commensurate antiferromagnetic (AFM) orders with a propagation vector $k = (0, \sim 0.5, 0)$, and the expansion of the Yafet-Kittel-type ferrimagnetic phase, becoming the only ground state. As a result, the magnetic ordering temperature T_N increases rapidly, from $\sim$43 K at $P = 0$ GPa to $\sim$100 K at $P = 10$ GPa. In the orthorhombic CaMn$_2$O$_4$-type phase, the AFM ordering on the sublattice of Mn^{3+} spins with a propagation vector $k = (1/2, 0, 0)$ occurs below $T_N = 275$ K for $P = 20$ GPa. This value of T_N is about six times greater than that obtained at ambient pressure for the tetragonal phase, indicating a strong pressure enhancement of the magnetic ordering temperature in Mn$_3$O$_4$. These experimental observations have been complemented by density functional theory calculations, which shed light on the underlying mechanisms of the structurally coupled magnetic phenomena in geometrically frustrated magnetic systems under high pressure.

I. INTRODUCTION

Spinel structured materials of AB_2O_4 have been a subject of great interest because of their potential technological applications as well as a wide variety of intriguing magnetic phenomena owing to geometrical frustration, including multiferroicity, spin-Peierls transitions, exotic magnetic states, spin-orbital liquids, and orbital glass behavior [1–6]. In the cubic spinel structure, A-site cations form a diamond sublattice while B-site ones form a pyrochlore lattice of corner-sharing

B_4 tetrahedra, each of which consists of six equivalent nearest-neighbor B-B bonds. If the magnetic interaction between nearest-neighboring B spins is antiferromagnetic (AFM), these AFM B-B bonds cannot simultaneously be satisfied, giving rise to a strong magnetic frustration [7,8].

The degeneracy among six B-B bonds within the B_4 tetrahedra as well as the geometrical frustration can be partially lifted by lattice distortions, as it occurs in the normal spinel Mn$_3$O$_4$. In this system, the Mn^{2+} and Mn^{3+} ions are located, respectively, at the tetrahedral (A) and octahedral (B) sites. The cooperative Jahn-Teller effect, related to the degeneracy of e_g orbitals of Mn^{3+} ions, causes elongation of MnO$_6$ octahedra along the c axis, resulting in lowering the crystal symmetry to a tetragonally distorted structure with space group $I4_1/amd$ as illustrated in Fig. 1. The tetragonal distortion leads to existence of two nonequivalent B-B exchange interactions with different Mn-Mn distances, in-plane J_{BBi}

---
*Corresponding authors: denk@nf.jinr.ru
†dangngoctoan1@duytan.edu.vn
‡ltpthao@ued.udn.vn
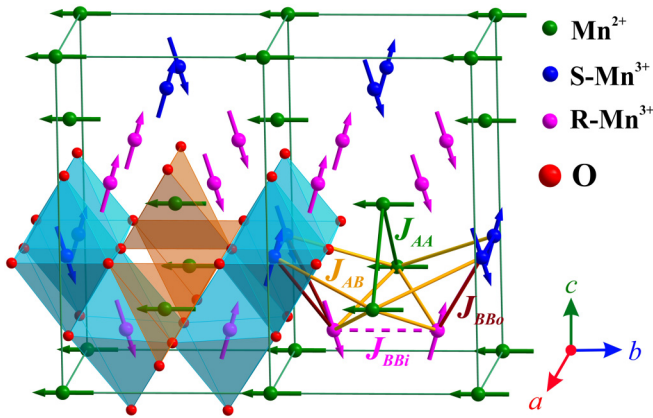§anhtt@hcmute.edu.vn
‖phanm@usf.edu

FIG. 1. Representation of crystal and magnetic structures of Mn_3O_4 at ambient pressure and below $T_{N3} \approx 33$ K. The paths of the J_{AA}, J_{AB}, in-plane J_{BBi}, and out-plane J_{BBo} magnetic interactions between the *A*-site and *B*-site Mn spins are shown.

and out-of-plane J_{BBo}. The in-plane J_{BBi} interaction involves the short distances between Mn^{3+} ions (~ 2.85 Å), and the strong overlap between half-filled t_{2g} orbitals leads to the dominant AFM direct exchange interaction, prevailing over the weaker superexchange one through oxygen. The pronounced increase of the out-of-plane Mn–Mn distance (~ 3.11 Å) and competing character of the direct and superexchange interactions weaken J_{BBo} significantly. Notably, the large exchange anisotropy J_{BBo}/J_{BBi} (~ 0.06 for Mn_3O_4) plays a key role in the formation of the magnetic ground states in these spinel-structured materials [9–11].

The additional *A-B* superexchange interaction is also relatively weak, $J_{AB}/J_{BBi} \sim 0.11$ [11]. The competition between the *A-B* and *B-B* magnetic interactions in Mn_3O_4 results in its complex magnetic ground state [12–15]. It has been reported that this compound undergoes three successive magnetic transitions at $T_{N1} \approx 43$ K, $T_{N2} \approx 39$ K, and $T_{N3} \approx 33$ K [12–15], which are accompanied by long-wavelength lattice modulations, indicative of the strong spin-lattice coupling [16]. Below T_{N1}, the formation of the long-range Yafet-Kittel-type ferrimagnetic (YK-FiM) order was observed. In this magnetic order, the Mn^{3+} spins at the octahedral sites lying in the *bc* plane are symmetrically canted with respect to the *b* axis, and the resulting magnetization of the Mn^{3+} spins is antiparallel to that of the Mn^{2+} spins, forming the ferromagnetic (FM) sublattice at the tetragonal sites [12–15]. The second transition at $T_{N2} \approx 39$ K is associated with the subdivision of the Mn^{3+} spins into two independent sublattices with different spin orders, named R and S [14,15]. The R and Mn^{2+} spins remain the same order as in the YK-FiM phase, whereas the S spins order in an incommensurate conical structure around the *b* axis with a propagation vector $k = (0, \sim 0.47, 0)$ [14,15]. At $T_{N3} \sim 33$ K, the S spin order becomes commensurate with $k = (0, 0.5, 0)$ recovering the coplanar structure as in the YK-FiM phase (see Fig. 1) [14,15]. However, the origin of the lowest-temperature magnetic phase transition has remained elusive. While previous works on single crystals of Mn_3O_4 revealed a weak orthorhombic lattice distortion at T_{N3} and attributed this to the appearance of the commensurate phase [16,17] due to the lifting of geometrical frustration, Lee

et al. have recently suggested that the enhanced orthorhombic distortion, caused by Co^{2+} and Cu^{2+} doping into Mn_3O_4, suppresses the commensurate phase in this material [7,18].

The formation mechanisms of the magnetic orders in Mn_3O_4 can be understood through high-pressure studies, exploring the response of magnetic properties on a controllable variation of structural parameters, modifying relevant magnetic interactions. To our best knowledge, a clear understanding of the high-pressure behavior of the structurally coupled magnetic phases in Mn_3O_4 is lacking, since previous studies concentrated mainly on aspects of the pressure-induced structural phase transitions [19–22]. It was reported that upon compression, bulk Mn_3O_4 transformed into the $CaMn_2O_4$-type *Pbcm* marokite structure at 11.5 GPa that stabilized up to 47.3 GPa, while its nanosized samples underwent an intermediate phase transformation into the $CaTi_2O_4$-type *Bbmm* structure at ~ 14.5 GPa before transforming to the stable marokitelike structure at higher pressures [19–22].

To shed more light on the underlying mechanisms of the magnetic phase transitions in Mn_3O_4, we have performed a thorough study of the crystal and magnetic structures of Mn_3O_4 at high pressures up to 37 and 20 GPa by means of x-ray and neutron powder diffraction, respectively. The experimental results are complemented by density fuctional theory (DFT) calculations of the electronic and magnetic properties of Mn_3O_4 under compression.

II. EXPERIMENTAL AND COMPUTATIONAL DETAILS

The Mn_3O_4 sample was prepared by the autocombustion procedure described in Ref. [23]. Analytical grade metal nitrite $Mn(NO_3)_2 \cdot 6H_2O$, urea $CO(NH_2)_2$, and sucrose $C_{12}H_{22}O$ used as initial fuels were dissolved in deionized water and mixed in an appropriate ratio to form a precursor solution. The mixed precursor solution was concentrated by heating until the excess free water was evaporated and spontaneous ignition appeared. The combustion happened within a few seconds and the resultant ash was collected. In order to increase crystallinity, the as-prepared sample was annealed at 1000 °C for 3 h in a box furnace.

The x-ray powder diffraction (XRD) experiments at high pressures up to 37 GPa were performed using the SAXS/WAXS Xeuss 3.0 system (XENOCS) and Dectris Eiger 2R 500 K detector, Mo K_α radiation ($\lambda = 0.7115$ Å). The Boehler-Almax Plate type diamond anvil cell was used in the experiments. The diamonds with culets of 300 μm were taken. The sample was loaded into the hole of the 150-μm diameter made in the Re gasket indented to about 30-μm thickness. The 4:1 methanol: ethanol mixture was used as a pressure transmitting medium. The two-dimensional XRD images were converted to one-dimensional diffraction patterns using the FIT2D program [24]. The pressure was measured using the ruby fluorescence technique and the typical determination error has not exceeded 0.1 GPa.

The neutron powder-diffraction (NPD) measurements at pressures up to 6.8 GPa were performed at selected temperatures in a range of $T = 15–300$ K with the DN-12 and DN-6 diffractometers (IBR-2 pulsed reactor, JINR, Russia) using a sapphire anvil high-pressure cell [25,26]. Diffraction patterns were collected at scattering angles of $2\theta = 45.5°$ and

90° with resolution of $\Delta d/d = 0.022$ and 0.015, respectively. Additional experiments in an extended pressure range up to 20 GPa were performed with the DN-6 diffractometer using a diamond anvil cell of the Boehler-Almax Plate type. The diffraction patterns were collected at the scattering angle of 90°. The pressure inside the sapphire and diamond anvil cells was measured using the ruby fluorescence technique. The pressure gradient was less than 10% with respect to the average pressure value. The XRD and NPD data were analyzed by the Rietveld method using the Fullprof program [27].

The *ab initio* DFT calculations have been performed using projector augmented-wave pseudopotentials treating ion-electron interactions as implemented in the Quantum-ESPRESSO *ab initio* software package [28,29]. Perdew-Burke-Ernzerhof approximation of the generalized gradient approximation (GGA) was used to describe the electronic exchange and correlation effects [30,31]. The GGA + U correction was used to correct for the strong correlation of $3d$ electrons in transition metals, where U was taken to be 5 eV for Mn. The electronic wave function was expanded in a plane wave basis set with an energy cutoff of 80 Ry. The charge density was expanded in a basis set with a 720 Ry plane wave cutoff. All relevant calculations were done on the conventional tetragonal $I4_1/amd$ unit-cell of Mn_3O_4 using an $8 \times 8 \times 5$ Monkhorst-Pack grid for the sampling of the Brillouin zone [32]. All ionic relaxations and cell optimizations were performed using a threshold of 10^{-5} Ry/Bohr for the force and 10^{-6} Ry for the unit cell energy. Bader charge analysis was performed based on the zero-flux surface of charge density [33] on relaxed structures at selected pressures. The strengths of the magnetic exchange interactions were calculated by mapping the total spin exchange energies of FM and six ferrimagnetic orderings as described in detail in Refs. [34,35]. The spin configurations of the magnetic orders are the same as those proposed by Chartier *et al.* [35].

III. RESULTS AND DISCUSSION

A. X-ray diffraction

The XRD patterns of Mn_3O_4 measured at room temperature and selected pressures up to 37 GPa are shown in Fig. 2. The Rietveld refinement of the experimental data at ambient conditions has revealed that the synthesized sample has a single-phase adopting the spinel tetragonal structure with $I4_1/amd$ symmetry and unit-cell parameters $a = b = 5.772(3)$ Å and $c = 9.462(6)$ Å, consistent with previous studies [15,36]. A good agreement between the experimental data and structural model was achieved with acceptable R factors, $R_f = 9.64\%$ and $R_B = 10.94\%$.

Upon compression, two structural phase transitions occurred. The first one takes place above $P = 10$ GPa, as evidenced by the appearance of additional diffraction peaks located at ~13.3° and ~16.6° (Fig. 2). The analysis has shown that these peaks, in an ascending order of their angular positions, correspond to the (111) and (301) reflections of the pressure-induced orthorhombic $CaTi_2O_4$-type phase with $Bbmm$ space group, with the unit-cell parameters $a = 10.70(2)$ Å, $b = 9.35(2)$ Å, and $c = 3.543(7)$ Å at 12.5 GPa, giving $R_f = 7.25\%$ and $R_B = 11.26\%$. A simi-
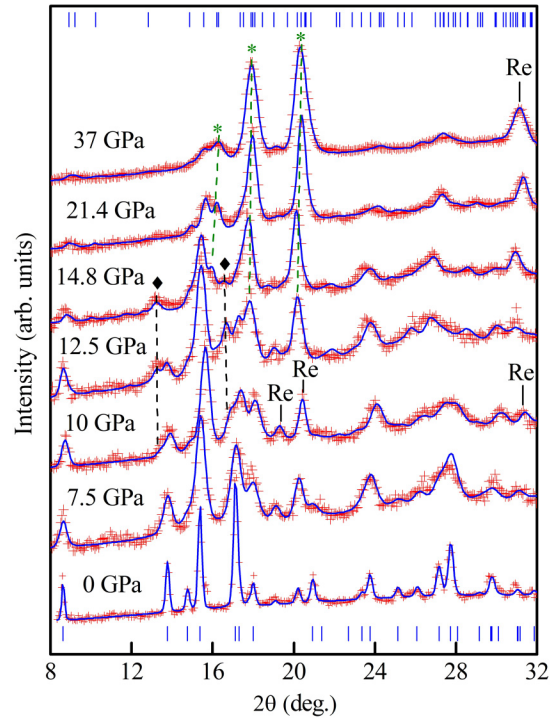

FIG. 2. Room-temperature x-ray diffraction patterns of Mn_3O_4 at selected pressures and processed by the Rietveld method. The experimental points and calculated profiles are shown. Vertical ticks at the bottom and top represent calculated positions of the nuclear peaks of the tetragonal $I4_1/amd$ and orthorhombic $Pbcm$ phases at 0 and 37 GPa, respectively. The symbols (♦) and (∗) denote diffraction peaks characteristic for the $Bbmm$ and $Pbcm$ orthorhombic phases, respectively.

lar structural transformation has recently been reported for Mn_3O_4 nanoparticles and nanorods [20,22]. On the other hand, above $P = 14.8$ GPa, an extra peak at ~15.9° and additional contribution to the intensity of nuclear peaks at ~17.9° and ~20.2° is observed, which rises significantly upon further compression. These observations imply the occurrence of a second structural phase transformation. The analysis has proved that the three peaks, in ascending order of their angular positions, correspond to the (023), (112), and (130) reflections of the second high-pressure marokite $CaMn_2O_4$-type phase of Mn_3O_4 with $Pbcm$ space-group, consistent with previous studies [19,20,22,37]. The Rietveld refinement involving the $Pbcm$ phase provided a satisfactory fit to the experimental data, for example, $R_f = 7.58\%$ and $R_B = 10.62\%$ for $P = 21.4$ GPa. Moreover, the lattice parameters of the marokite phase obtained from the refinement of both XRD and NPD data at $P = 20$ GPa are $a = 2.865(3)$ Å, $b = 9.426(9)$ Å, and $c = 9.368(11)$ Å, which are in good agreement with previous studies [20,22,37]. The pressure evolutions of the weight fraction of the polymorphs of Mn_3O_4 have been established, and the results are presented in Fig. 3.

B. Neutron diffraction

Further, to elucidate the mechanism underlying the magnetic phase transitions in the tetragonal phase of Mn_3O_4, NPD
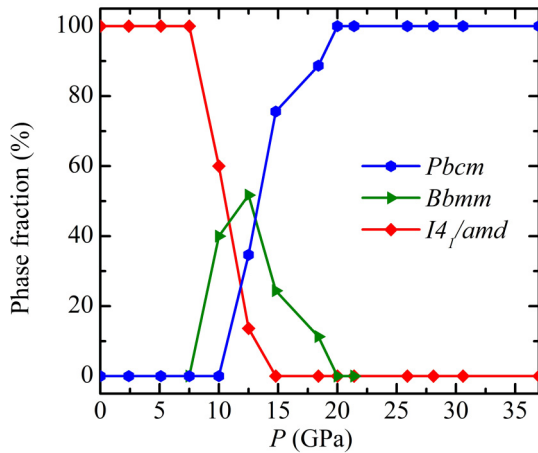
FIG. 3. Pressure dependence of phase weight fraction in Mn_3O_4.

patterns were collected at low temperatures and pressures up to 10 GPa, where the tetragonal phase predominates. Fig. 4(a) presents the temperature evolution of the NPD pattern of Mn_3O_4 at ambient pressure. The data analysis has revealed that the tetragonal crystal structure remains unchanged in the entire studied temperature range, which is consistent with the previous studies of polycrystalline Mn_3O_4 [7,14,15,18,38]. Moreover, below $T_{N1} = 43$ K, an appearance of magnetic contribution to the intensity of nuclear peaks located at d_{hkl} positions of 3.08, 4.07, and 4.91 Å was observed (Fig. 4). The data analysis has shown that this appearance corresponds to the formation of the YK-type ferrimagnetic order, giving $R_f = 2.93\%$, $R_B = 6.32\%$, and the magnetic R-factor $R_M = 12.9\%$ for $T = 41$ K. Upon further cooling, at $T = 35$ K

new magnetic peaks appeared at d_{hkl} positions of 4.59 and 5.10 Å, corresponding to the appearance of the incommensurate part of the S spins with $k = (0, 0.45, 0)$ (see Fig. 4). For the incommensurate part, Chardon *et al.* reported the sinusoidal spin structure, where only the z component of the S spins is modulated along the b axis [15]. In contrast, Jensen *et al.* [38] proposed the conical spin structure along the b direction, which was supported by magnetocapacitance measurements [13]. After consideration of both models, we have found that the data are best fitted to the conical model ($R_f = 3.22\%$, $R_B = 7.65\%$, and $R_M = 11.8\%$ for $T = 35$ K). With further decrease in the temperature, at $T = 30$ K the S spin order becomes commensurate with $k = (0, 0.5, 0)$ as detected by the shift of its characteristic magnetic peaks compared to those at $T = 35$ K [see Fig. 4(b)]. The corresponding R-factors for the commensurate magnetic model are $R_f = 2.15\%$, $R_B = 6.28\%$, and $R_M = 10.5\%$ for $T = 21$ K. The ordered magnetic moments at $T = 21$ K are 3.2(1) and 2.6(1) μ_B for the A and B sites, respectively. Notably, these values are smaller than the spin-only ones for the high-spin Mn^{2+} and Mn^{3+} ions, indicating the existence of a large fraction of disordered Mn spins.

The temperature evolution of lattice parameters and Mn-O bond lengths of the tetragonal phase has been established and listed in Supplemental Material Table S1 [39]. Below $T_{N1} = 43$ K, the parameter c increases remarkably with decreasing temperature, while the parameters a and b ($a = b$) slightly decrease with a minimum at 30 K (see Table S1) [39]. Furthermore, the MnO_6 octahedra become more distorted with a significant elongation of the apical Mn^{3+}-O_{ap} bond lengths upon cooling, while the equatorial Mn^{3+}-O_{eq} bond lengths remain nearly temperature independent [Fig. 4(c)]. On the other hand, the Mn-O bond lengths of the MnO_4 tetrahedra are
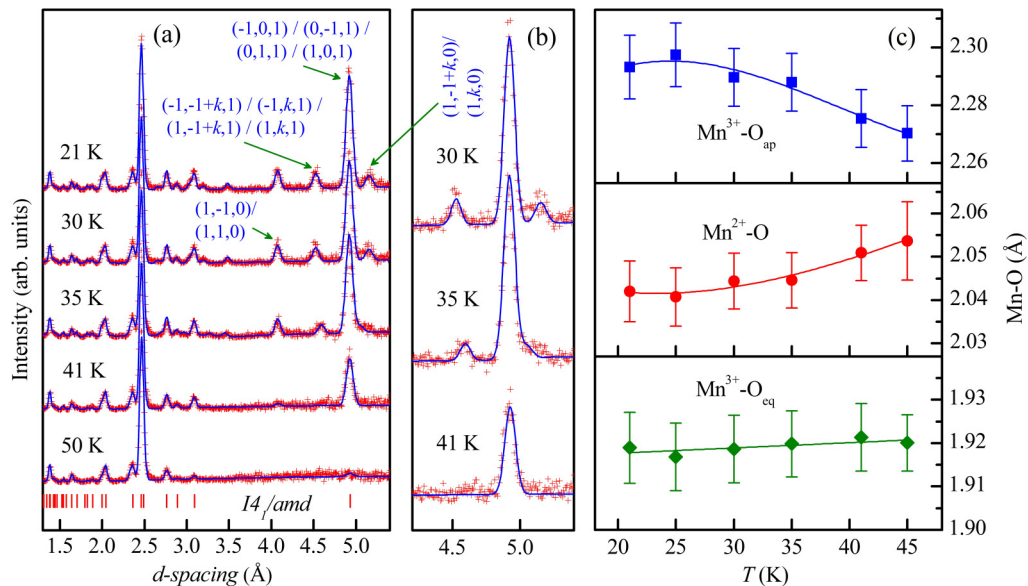

FIG. 4. (a) Low-temperature NPD patterns of Mn_3O_4 at ambient pressure. (b) The enlarged section of the pattern region containing characteristic magnetic peaks of the conical order of the S-spin sublattice. The experimental points and calculated profiles processed by the Rietveld method are shown. Vertical ticks below represent calculated positions of the nuclear peaks of the tetragonal $I4_1/amd$ phase. Indices of the most intense magnetic peaks are shown. (c) The temperature dependences of Mn-O interatomic distances. The lines are guides for eyes only.
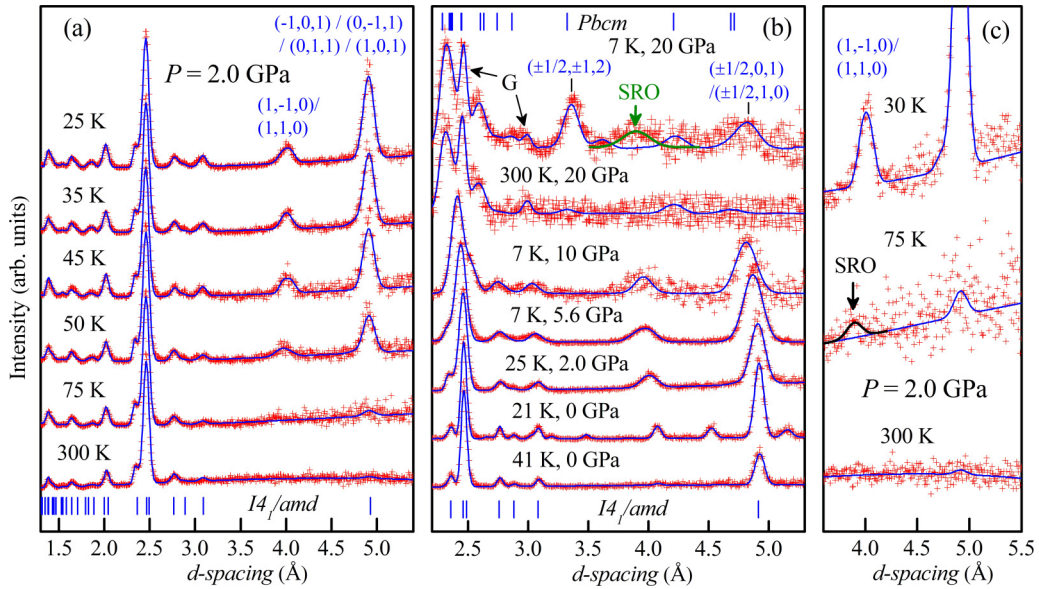
FIG. 5. (a) NPD patterns of Mn_3O_4 at 2 GPa as a function of temperature. (b) Neutron diffraction patterns of Mn_3O_4 at selected temperatures and pressures. The experimental points and calculated profiles processed by the Rietveld method are shown. Vertical ticks represent calculated positions of nuclear reflections of corresponding structural phases. Indices of the most intense magnetic peaks are shown. The background peak from the diamond anvil cell is denoted by the symbol "G" in panel (b). The symbol SRO denotes the magnetic short-range order. (c) An enlarged section of the NPD patterns at 2 GPa, demonstrating the evolution of the short-range magnetic order.

reduced remarkably with decreasing temperature [Fig. 4(c)]. Such changes in the structural parameters are expected to alter the balance between the magnetic interactions and hence the magnetic phase transitions.

As aforementioned, the magnetic frustration degree, as well as features of the magnetic ground states in the studied spinel, is controlled by the competition between the A-B and in- and out-of-plane B-B magnetic interactions. To get more insight into the nature of the observed magnetic phenomena, the values of the magnetic exchange interactions as a function of temperature have been calculated by mapping the total spin-exchange energies of different collinear spin configurations from DFT+U calculations adopting the experimental structural data at 45, 41 and 21 K [34,35,40]. The obtained values of magnetic interaction strengths are $J_{AA} = 0.96$ K, $J_{AB} = -40.00$ K, $J_{BBo} = -31.28$ K, and $J_{BBi} = -242.50$ K at 45 K, which are comparable with those previously reported in Ref. [34]. Across the first magnetic transition T_{N1}, the J_{BBi} magnetic interaction weakens, while the others significantly strengthen. Their values at 41 K are $J_{AA} = -2.92$ K, $J_{AB} = -43.53$ K, $J_{BBo} = -33.52$ K, and $J_{BBi} = -240.48$ K. The larger enhancement of J_{AB} compared to the average B-B magnetic interaction reduces the magnetic frustration, favoring the formation of the long-range YK-type FiM order. Upon further cooling, J_{BBi} remains almost unchanged ($J_{BBi} = -240.82$ K at 21 K), while J_{BBo} displays a larger enhancement compared to J_{AB} ($J_{BBo} = -36.39$ K and $J_{AB} = -45.86$ K at 21 K). The observations indicate that the enhanced ratio J_{BBo}/J_{AB} is a possible reason for the appearance of the conical order of the S-spin sublattice below T_{N2}.

Under compression at $P = 2$ GPa, a full suppression of the magnetic peaks of the individual commensurate/incommensurate order of the S spins is observed, evidencing a magnetic structure transformation (Fig. 5). The

data refinement has shown that the high-pressure magnetic phase has the same YK-FiM structure as observed at ambient pressure. The YK-FiM magnetic phase, which becomes a single magnetically ordered state, is stable upon increasing pressure up to 10 GPa. On the other hand, it has been recently found that similar magnetic phenomena observed under compression can be also caused by Co or Cu doping into Mn_3O_4 [7,18], which have been ascribed to the tetragonal-to-orthorhombic structural transition. Additionally, the orthorhombic distortion under compression in Mn_3O_4 has been suggested from the single-crystal Raman scattering measurements [41,42]. However, we have observed no sign of change in the crystal structure in the neutron diffraction pattern in the temperature range of 25–300 K [Fig. 5(a)], implying the stability of the tetragonal phase. The agreement between the tetragonal YK-FiM model and high-pressure experimental data can be evidenced by the good values of R factors, for example, $R_f = 10.7\%$, $R_B = 9.3\%$ and $R_M = 8.8\%$ for $T = 25$ K and $P = 2$ GPa. The observation suggests an alternative mechanism that underlies the pressure-induced magnetic transitions in Mn_3O_4, which is discussed further below using our *ab initio* DFT calculations.

At high pressures in the paramagnetic region, a formation of short-range magnetic correlations was also realized. At $P = 2$ GPa and $T = 75$ K apparent magnetic diffuse peak at $d \approx 3.95$ Å appeared [Fig. 5(c)], close to the position of the magnetic peak (1 1 0)/(1 -1 0) of the FiM order forming below $T_N = 60$ K. As the (110)/(1-10) peak intensity is associated with the antiferromagnetic arrangement of the z component of the Mn^{3+} spins, it is reasonable to ascribe the diffuse scattering to the short-range spin correlations in the Mn^{3+} sublattice. The magnetic correlation length for the short-range ordered phase is evaluated by the Selyakov-Scherrer formula ($\xi \approx d_{sro}^2 / \Delta d_{sro}$) using the position ($d_{sro}$) and the full width
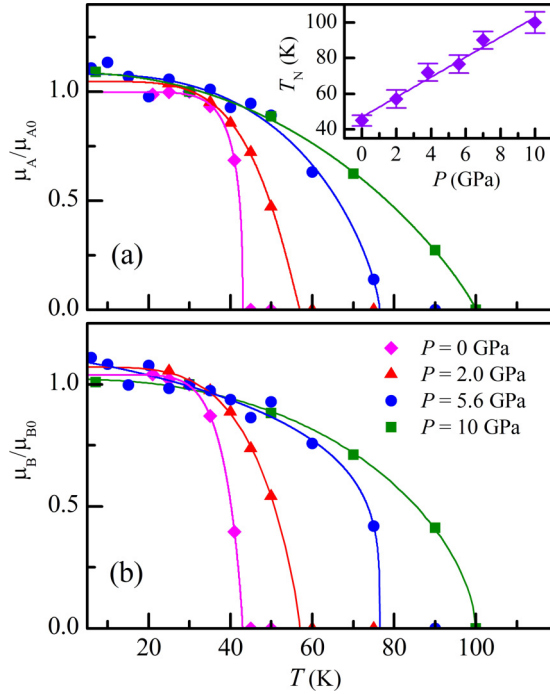
FIG. 6. Temperature dependences of the ordered Mn magnetic moments at the A (a) and B (b) sites of Mn_3O_4 normalized to those obtained at $T = 30$ K at selected pressures and their interpolations by the functions $\mu(T) = \mu_0(1 - (T/T_N)^\alpha)^\beta$. Inset: Pressure dependence of the ordering temperature T_N of Mn_3O_4 and its linear interpolation.

FIG. 7. Representation of the crystal and magnetic structures of the orthorhombic *Pbcm* phase of Mn_3O_4 at 20 GPa. The path of the Mn^{3+}-O-Mn^{3+} superexchange interaction connecting the one-dimensional zigzag AFM chains of Mn^{3+} spins are denoted by black solid lines.

at half-maximum (Δd_{sro}) of the relevant magnetic peak [43]. Using the experimental data, the values of ξ are calculated for all measured pressures. The value of ξ of 105 Å is found to be weakly pressure-dependent in the pressure range up to 7 GPa. At $P = 10$ GPa, the diffuse peak was no longer detected [Fig. 5(b)], suggesting the suppression of the short-range magnetic order.

The temperature dependences of the magnetic moments at two Mn sites at each pressure are established and evaluated by fitting the $\mu_{AFM}(T)$ data by the function: $\mu(T) = \mu_0(1 - (T/T_N)^\alpha)^\beta$, where μ_0 is the magnetic moment at $T = 0$ K, T_N (T_{N1} for $P = 0$ GPa, T_N for $P > 2$ GPa) is the magnetic ordering temperature, and α and β are fitting parameters (Fig. 6). Under pressures up to 10 GPa, the magnetic ordering temperatures of the A and B magnetic sublattices coincide and increase significantly in about 2.5 times from 43(2) K at $P = 0$ GPa to 100(5) K at $P = 10$ GPa with the pressure coefficient $dT_N/dP = 5.7(5)$ K/GPa. It is worth noting that the normalized value $(1/T_N)(dT_N/dP) = 0.132$ GPa^{-1} is much larger than those obtained for other spinels Co_3O_4 (0.0091 GPa^{-1}) [44], $Zn_{0.3}Cu_{0.7}Fe_{1.5}Ga_{0.5}O_4$ (0.048 GPa^{-1}) [45], implying a strong pressure-induced enhancement of magnetic interactions in the case of Mn_3O_4.

Because of the phase coexistence, it was difficult to analyze the magnetic properties of the high-pressure intermediate orthorhombic *Bbmm* phase of Mn_3O_4. To investigate the magnetic structure of the orthorhombic *Pbcm* phase of Mn_3O_4, the low-temperature NPD patterns were collected at pressure of 20 GPa. It has been found that the orthorhombic *Pbcm*
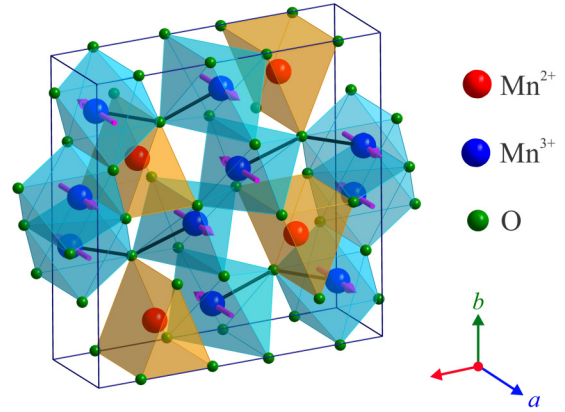
crystal structure remained unchanged upon cooling down to 7 K. On the other hand, below $T_N = 275$ K, there was an emerging appearance of the magnetic peaks at $d_{hkl} = 3.36$ and 4.83 Å [Fig. 5(b)]. The data analysis has revealed that the peak corresponds to the formation of the AFM magnetic order of Mn^{3+} spins with a propagation vector $k = (1/2, 0, 0)$, whose features are shown in Fig. 7. The experimental NPD data are well fitted by this model, for instance at $T = 7$ K and $P = 20$ GPa the R-factors are $R_f = 5.64\%$, $R_B = 10.7\%$ and $R_M = 15.6\%$. It should be mentioned that such a magnetic structure is similar to that found in isostructural $CaMn_2O_4$ [46]. It is also consistent with the results of the study on the metastable *Pbcm* phase of Mn_3O_4, synthesized under high pressure and temperature conditions and recovered to ambient pressure by slow decompression [47].

In the *Pbcm* orthorhombic structure, Mn^{3+} ions with octahedral oxygen coordination form one-dimensional edge-sharing chains along the a axis with zigzag arrangement along the b axis, while Mn^{2+} ions with eightfold oxygen coordination are located in channels arranged by the network of these chains (Fig. 7). The predominant AFM direct exchange between Mn^{3+} ions of neighboring edge-sharing octahedra leads to the formation of the AFM chains of Mn^{3+} spins along the a and b axes. Furthermore, the zigzag chains are coupled via the AFM Mn^{3+}-O-Mn^{3+} superexchange interactions of corner-sharing octahedra (Fig. 7), forming the three-dimensional long-range antiferromagnetic order on the Mn^{3+} sublattice.

The lifting of magnetic frustration on the Mn^{3+} magnetic sublattice in the *Pbcm* phase along with the pressure-induced enhancement of magnetic interactions leads to a giant increase of the magnetic ordering temperature by more than 6 times from 43 K at ambient pressure to 275 K at 20 GPa. The latter value (275 K) is also about 30% greater with respect to $T_N = 210$ K reported for the metastable orthorhombic *Pbcm* phase of Mn_3O_4 at ambient pressure [44]. The Mn^{2+} ions are surrounded by honeycomb arrangements of Mn^{3+} ions, preventing the formation of the long-range magnetic order on the Mn^{2+} sublattice [44]. Below 50 K, the emergence of a new broad magnetic peak located at $d_{hkl} = 3.89$ Å was detected
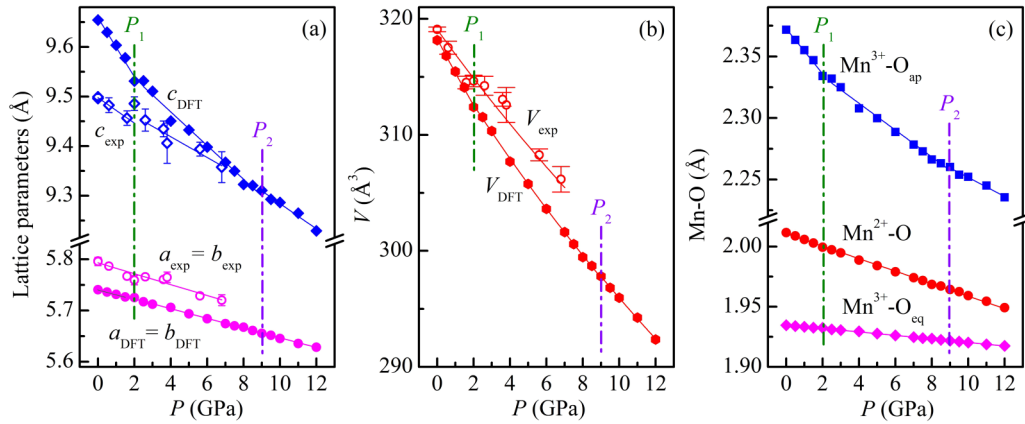
FIG. 8. Evolutions of calculated unit-cell parameters (a), volume (b), and bond lengths Mn-O (c) of the tetragonal phase of Mn_3O_4 (denoted by solid symbols) as functions of pressure and their interpolations using the Birch-Murnaghan equation of state. The experimental values of the room-temperature lattice parameters at selected pressures are denoted by open symbols in (a) and (b). Vertical dashed lines mark the pressure points of the isostructural phase transitions.

(Fig. 5), which is likely associated with the presence of the short-range magnetic order of Mn^{2+} ions. The magnetic correlation length, estimated using the Selyakov-Scherrer formula [43], is about 57 Å.

C. DFT calculations

Since DFT calculations for complex magnetic configurations require very large computational resources, their performance for the experimentally observed magnetic structures of Mn_3O_4 would become more challenging. Therefore, the *ab initio* DFT calculations have been performed using the collinear FiM tetragonal phase with all A and B spins aligned along the b axis in the pressure range up to 12 GPa for clarifying the nature of the experimentally observed pressure-induced magnetic transitions in the tetragonal phase of Mn_3O_4, which is similar to the procedure used in previous DFT studies on Mn_3O_4 and other spinel compounds [9,34,35,48–51]. At ambient pressure, the calculated lattice parameters of Mn_3O_4 are $a = b = 5.7407$ Å and $c = 9.6543$ Å. The calculated interatomic distances of Mn^{3+}-O_{ap}, Mn^{2+}-O, and Mn^{3+}-O_{eq} are 2.37 Å, 2.01 Å, and 1.93 Å, respectively. The obtained results are comparable with those from our experimental measurements (Fig. 4) and the previous DFT calculations [52].

The pressure dependences of the calculated structural parameters are shown in Fig. 8. It is important to mention that the DFT calculations have predicted the occurrence of two isostructural transformations around $P_1 = 2.0$ GPa and $P_2 = 9.0$ GPa, evidenced by noticeable changes of the lattice parameter c. Particularly, the average compressibility $k_c = -(1/c_0)(dc/dP)_T$ abruptly reduces from 0.0053 to 0.0035 GPa^{-1} at P_1 and then to 0.0026 GPa^{-1} at P_2. Notably, the pressure point of the first isostructural transition is close to that of the magnetic transition at $P \sim 2$ GPa, implying a noticeable spin-lattice coupling. The parameters a and b ($a = b$) smoothly decrease throughout the investigated pressure range with the coefficient $k_a = k_b = 0.0017$ GPa^{-1}, which is much smaller than k_c. This indicates an anisotropic

lattice compression with the c axis being the most compressible. The Mn^{3+}-O_{ap} bond lengths also show anomalies across the isostructural phase transitions, while the Mn^{3+}-O_{eq} and Mn^{2+}-O ones continuously decrease in the investigated pressure range. As can be seen in Fig. 8(c), the Mn^{3+}-O_{ap} and Mn^{3+}-O_{eq} bonds are the most and least compressible.

For comparison, the experimental values of the room-temperature lattice parameters of the tetragonal phase as a function of pressure are also presented in Fig. 8. The trends between the calculated and experimental structural parameters under compression are quite similar. It should be noted that the anisotropic lattice compression and anomalous changes of the lattice parameters around 2 GPa were also detected earlier [19,20]. The volume compressibility data are fitted to the third-order Birch-Murnaghan equation of state [53]: $P = \frac{3}{2}B_0(x^{-7/3} - x^{-5/3})[1 + \frac{3}{4}(B' - 4)(x^{-2/3} - 1)]$, where $x = V/V_0$ is the relative volume change, V_0 is the unit cell volume at $P = 0$ GPa, and B_0, B' are the bulk modulus ($B_0 = -V(dP/dV)_T$) and its pressure derivative ($B' = (dB_0/dP)_T$) fixed at 4.0. Fitting the theoretical data, the bulk modulus value B_0 demonstrates an increase from 106(4) GPa to 122(1) GPa across the first isostructural transition, and then slightly increases to 124(4) GPa at the second one. These values are somewhat smaller than the experimental one of 155(8) GPa. Notably, the obtained experimental value B_0 is comparable to ones $B_0 = 168$ and 154 GPa found for bulk and nanorods of Mn_3O_4, and much smaller than that of Mn_3O_4 nanoparticles with $B_0 = 202$ GPa [19,20,22].

Furthermore, the pressure dependence of the magnetic exchange interactions has been established and the corresponding parameters are listed in Table I. It can be seen in Fig. 9 that all the magnetic interactions strengthen upon compression as a direct result of the shrinkage of the lattice. It can be derived from Fig. 9 that the J_{BBo}/J_{AB} ratio remains nearly unchanged under compression up to 2 GPa (see the inset of Fig. 9), and then quickly decreases with further compression up to 12 GPa. The decrease of J_{BBo}/J_{AB} releases the magnetic frustration, leading to the magnetic transformation from the incommensurate/commensurate phase to the YK-FiM one in

TABLE I. Calculated magnetic exchange interaction constants J_{AA}, J_{AB}, J_{BBo} and J_{BBi} of the tetragonal phase of Mn_3O_4 at different pressures.

P (GPA)	J_{AA} (K)	J_{AB} (K)	J_{BBo} (K)	J_{BBi} (K)
0	−20.92	−51.23	−36.95	−220.13
0.5	−21.4l	−52.17	−37.6	−223.13
1.0	−21.90	−53.13	−38.27	−226.26
1.5	−22.39	−54.15	−38.96	−229.61
2.0	−23.12	−55.13	−39.84	−232.88
4.0	−24.78	−59.12	−42.25	−246.43
6.0	−25.89	−63.18	−44.24	−260.82
8.0	−26.92	−67.20	−46.17	−275.78
10	−27.41	−71.41	−47.63	−291.66
12	−27.60	−75.63	−48.88	−308.94

Mn_3O_4 under pressure. Moreover, the larger enhancement of J_{AB} compared to J_{BBo} and J_{BBi} explains the stabilization of the YK-FiM phase upon compression. The observations affirm the suggestion about the key role of the ratio J_{BBo}/J_{AB} on the magnetic properties of Mn_3O_4.

To elucidate the nature of the pressure-induced magnetostructural transition, the pressure dependence of the Bader charge on each constituent atom of the tetragonal unit cell of Mn_3O_4 has been established. As can be seen in Fig. 10, the atomic Bader charge curves demonstrate notable anomalies around the structural transitions, implying the electronic origin of the pressure-induced isostructural transformations in Mn_3O_4. For instance, under compression up to 2 GPa, the Bader charges of Mn ions at both octahedral and tetrahedral sites linearly increase, and those of O ions decrease, implying a negative charge transfer from Mn ions to O ones. Above
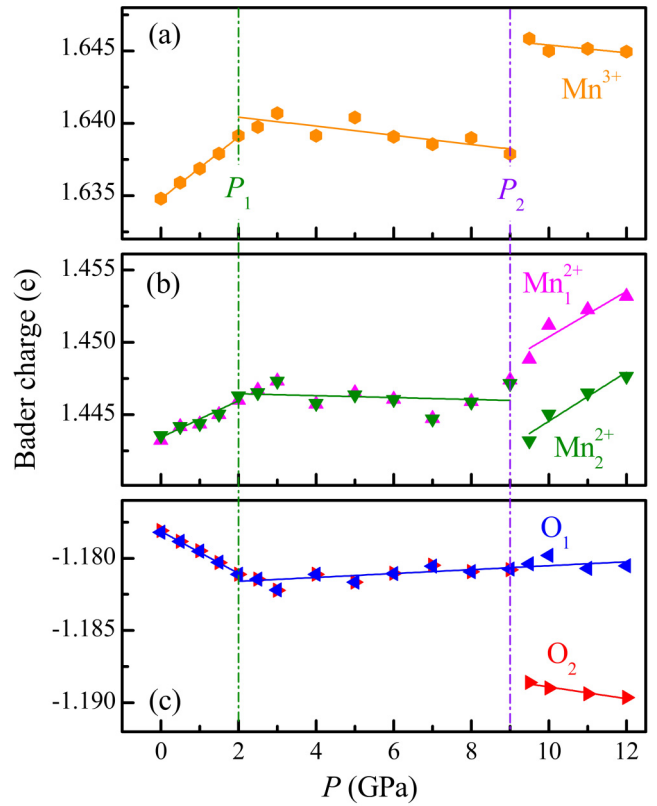
FIG. 10. Pressure dependences of average Bader charges of Mn at octahedral (a) and tetrahedral (b) sites and O (c) atoms in Mn_3O_4. Vertical dashed lines mark the pressure points of the isostructural phase transitions.

2 GPa, the Bader charges of Mn ions start to decrease with increasing pressure while the charges on O ions increase slightly. It provides solid evidence for the charge transfer from O ions to Mn ones.

Other anomalies of interest are also observed on the Bader charge curves around the second isostructural transformation point $P_2 = 9$ GPa (Fig. 10). Below 9 GPa, all Mn^{2+} ions at A sites have the same Barder charge whereas above 9 GPa they split into two groups with nonequivalent Bader charges. The Bader charges of two Mn^{2+} ions (group 1), occupying the origin and the center of the unit cell, increase abruptly at 9 GPa while those of two remaining Mn^{2+} ions (group 2) demonstrate an abrupt reduction. Simultaneously, the Bader charges of all apical oxygen ions in MnO_4 tetrahedra of the first group Mn^{2+} ions exhibit an abrupt decrease beyond the phase transition while those of O ions in MnO_4 tetrahedra of the second group Mn^{2+} ions do not show any significant changes. On the contrary, the Bader charges of all Mn^{3+} ions at the octahedral sites are the same in the pressure range up to 12 GPa with an abrupt increase at the transition point. The electronic origin of the magnetostructural transition can be explained by the anomalies observed in the pressure dependences of Bader atomic charges. These anomalies indicate anomalous modifications in the configuration of bonding electrons, causing changes in interatomic interactions and structural parameters. A similar mechanism has been reported for isostructural phase
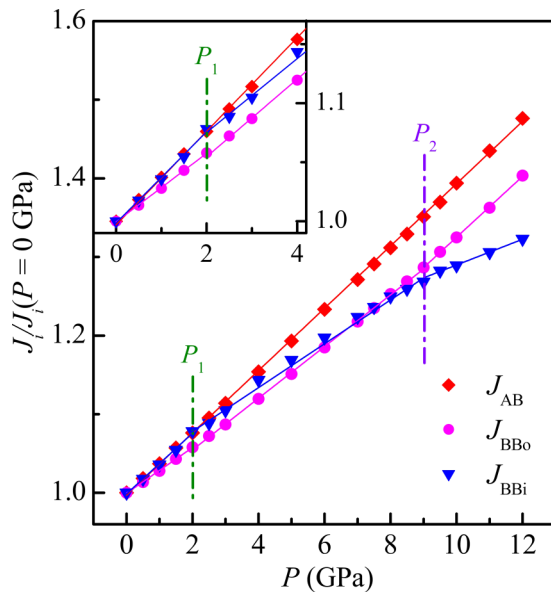

FIG. 9. Pressure dependence of magnetic interaction strengths normalized by their ambient pressure values. The inset shows an enlarged zoom of the low-pressure region. Vertical dashed lines mark the pressure points of the isostructural phase transitions.
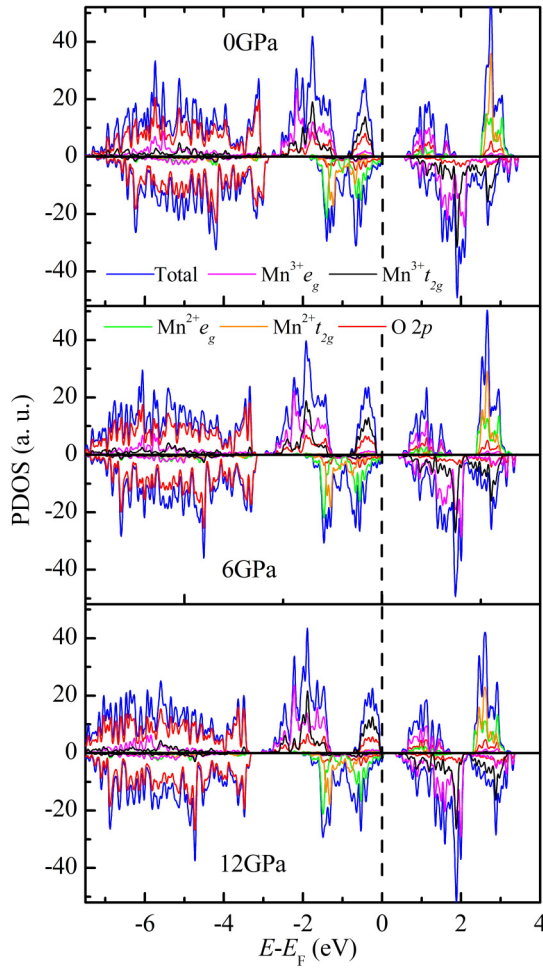
FIG. 11. Partial density of states (PDOS) plotted in the two spin directions of Mn_3O_4 at different pressures: (a) 0 GPa, (b) 6 GPa, and (c) 12 GPa.

transitions under compression observed in other compounds [54–56].

In order to investigate the behavior of the electronic structure of Mn_3O_4 upon compression, we have evaluated the partial density of states (PDOS) in the two spin directions of Mn_3O_4 at three selected pressures of 0, 6, and 12 GPa (Fig. 11). As can be seen in Fig. 11, in the spin-up configuration, the conduction band near the Fermi level is mainly contributed from the Mn^{3+} e_g orbitals. Meanwhile, the valence band is mostly composed of the Mn^{3+} t_{2g} orbitals. The O $2p$ orbitals also have an important contribution to the formation of electronic bands, especially the valence band. For the spin-down configuration, the contribution of Mn^{2+} e_g orbitals to the electronic bands is dominant. A predominant contribution of the O $2p$ orbitals is observed in the energy range from -3 to -6 eV of the valence band. In both spin channels, hybridization between cation $3d$ and O $2p$ orbitals is significant, which may lead to different crystal field splitting effects of cation $3d$ orbitals and thus affect the electron occupancy.

The system is characterized by large exchange splittings: near 4 eV for the tetrahedral A site (occupied by Mn^{2+}) and near 3 eV for the octahedral B site (occupied by Mn^{3+}).

Both sites are completely spin-polarized with the crystal field configurations as indicated in the caption of the figure. The Jahn-Teller distortion at the octahedral B site manifests clearly in the up-spin channel, which is seen to comprise filled t_{2g} states centered around -1.8 eV and separated from a filled d_{x2-y2} state just near -0.4eV. The empty down d_{z2} states are centered near 1.8 eV. The down Mn d states at the B site are all empty and found starting at 0.6 eV. Overall, the general shape of the PDOS almost does not change upon compression. The application of external pressure just causes the broadening of the electronic bands due to lattice shrinkage, resulting in a decrease of the bandgap.

Finally, it should be noted that it is challenging to perform DFT calculations for the pressure-induced orthorhombic phase using the described approach due to its structural complexity, and is beyond the scope of the present study. It will be a subject for further theoretical studies.

IV. CONCLUSIONS

In summary, the pressure-induced behaviors of the magnetic and crystal structures of the normal spinel Mn_3O_4 have been explored by the combination of experimental XRD and NPD techniques and *ab initio* DFT calculations. A sequence of the structural phase transitions from the initial tetragonal hausmannite to the orthorhombic $CaMn_2O_4$-type *Pbcm* marokite structure via the intermediate orthorhombic $CaTi_2O_4$-type *Bbmm* one was observed. In the tetragonal phase, the initial low temperature incommensurate and commensurate magnetic phases are suppressed under pressure, and the only YK-type phase is formed at $P > 2$ GPa. The magnetic ordering temperature increases rapidly from 43 to 100 K in the 0–10 GPa range due to the enhancement of magnetic interactions and the weakening of magnetic frustration effects.

Our DFT studies also predict an isostructural phase transformation at $P = 2$ GPa around the magnetic transition point, highlighting the magnetostructural coupling effect. The pressure-induced magnetic phase transitions in the tetragonal structural phase arise from the change in the J_{BBo}/J_{AB} magnetic interaction ratio.

Concerning the high-pressure orthorhombic $CaMn_2O_4$-type *Pbcm* phase, the Mn^{3+} spins demonstrate a long-range antiferromagnetic order with a propagation vector $k = (1/2, 0, 0)$, while the Mn^{2+} ions exhibit a short-range order. The corresponding Néel temperature at 20 GPa, $T_N = 275$ K, is nearly an order of magnitude larger than that reported for the tetragonal phase at ambient pressure ($T_N = 43$ K). This occurs due to the suppression of the magnetic frustration on the Mn^{3+} sublattice and the enhancement of magnetic interactions in the pressure-induced orthorhombic phase. Further theoretical studies are needed to shed light on the microscopic mechanism of the magnetic order formation in the orthorhombic phase.

[1] M. Kim, X. M. Chen, Y. I. Joe, E. Fradkin, P. Abbamonte, and S. L. Cooper, Phys. Rev. Lett. **104**, 136402 (2010).

[2] V. Tsurkan, H.-A. Krug von Nidda, J. Deisenhofer, P. Lunkenheimer, and A. Loidl, Phys. Rep. **926**, 1 (2021).

[3] V. Kocsis, S. Bordács, D. Varjas, K. Penc, A. Abouelsayed, C. A. Kuntscher, K. Ohgushi, Y. Tokura, and I. Kézsmárki, Phys. Rev. B **87**, 064416 (2013).

[4] V. Fritsch, J. Hemberger, N. Büttgen, E.-W. Scheidt, H.-A. Krug von Nidda, A. Loidl, and V. Tsurkan, Phys. Rev. Lett. **92**, 116401 (2004).

[5] R. Fichtl, V. Tsurkan, P. Lunkenheimer, J. Hemberger, V. Fritsch, H. A. Krug von Nidda, E. W. Scheidt, and A. Loidl, Phys. Rev. Lett. **94**, 027601 (2005).

[6] K. Singh, A. Maignan, C. Simon, and C. Martin, Appl. Phys. Lett. **99**, 172903 (2011).

[7] K. H. Lee, H. Chang, I. Y. Hwang, J.-H. Chung, H. W. Kang, S. J. Kim, and S. Lee, Phys. Rev. B **91**, 064404 (2015).

[8] J.-H. Chung, K. Hwan Lee, Y.-S. Song, T. Suzuki, and T. Katsufuji, J. Phys. Soc. Jpn. **82**, 034707 (2013).

[9] D. Das, R. Biswas, and S. Ghosh, J. Phys.: Condens. Matter **28**, 446001 (2016).

[10] J.-H. Chung, M. Matsuda, S.-H. Lee, K. Kakurai, H. Ueda, T. J. Sato, H. Takagi, K.-P. Hong, and S. Park, Phys. Rev. Lett. **95**, 247204 (2005).

[11] J.-H. Chung, J.-H. Kim, S.-H. Lee, T. J. Sato, T. Suzuki, M. Katsumura, and T. Katsufuji, Phys. Rev. B **77**, 054412 (2008).

[12] F. Guillou, S. Thota, W. Prellier, J. Kumar, and V. Hardy, Phys. Rev. B **83**, 094423 (2011).

[13] T. Suzuki and T. Katsufuji, Phys. Rev. B **77**, 220402(R) (2008).

[14] B. Boucher, R. Buhl, and M. Perrin, J. Appl. Phys. **42**, 1615 (1971).

[15] B. Chardon and F. Vigneron, J. Magn. Magn. Mater. **58**, 128 (1986).

[16] Y. Nii, H. Sagayama, H. Umetsu, N. Abe, K. Taniguchi, and T. Arima, Phys. Rev. B **87**, 195115 (2013).

[17] M. Kim, X. M. Chen, X. Wang, C. S. Nelson, R. Budakian, P. Abbamonte, and S. L. Cooper, Phys. Rev. B **84**, 174424 (2011).

[18] K. H. Lee, I. Y. Hwang, J.-H. Chung, H. Ishibashi, Y. Kubota, S. Kawaguchi, S. Lee, S. Torii, M. Hagihala, and T. Kamiyama, Phys. Rev. B **101**, 085126 (2020).

[19] J. Darul, C. Lathe, and P. Piszora, J. Phys. Chem. C **117**, 23487 (2013).

[20] H. Lv, M. Yao, Q. Li, Z. Li, B. Liu, R. Liu, S. Lu, D. Li, J. Mao, X. Ji, J. Liu, Z. Chen, B. Zou, T. Cui, and B. Liu, J. Phys. Chem. C **116**, 2165 (2012).

[21] X. J. Liu, S. Xu, K. Kato, and Y. Moritomo, J. Phys. Soc. Jpn. **71**, 2820 (2002).

[22] J. Li, B. Liu, J. Dong, C. Li, Q. Dong, T. Lin, R. Liu, P. Wang, P. Shen, Q. Li, and B. Liu, Nanoscale Adv. **2**, 5841 (2020).

[23] B. Chen, G. Rao, S. Wang, Y. Lan, L. Pan, and X. Zhang, Mater. Lett. **154**, 160 (2015).

[24] A. P. Hammersley, S. O. Svensson, M. Hanfland, A. N. Fitch, and D. Häusermann, High Press. Res. **14**, 235 (1996).

[25] V. L. Aksenov, A. M. Balagurov, V. P. Glazkov, D. P. Kozlenko, I. V. Naumov, B. N. Savenko, D. V. Sheptyakov, V. A. Somenkov, A. P. Bulkin, V. A. Kudryashev, and V. A. Trounov, Phys. B **265**, 258 (1999).

[26] D. Kozlenko, S. Kichanov, E. Lukin, and B. Savenko, Cryst. **8**, 331 (2018).

[27] J. Rodríguez-Carvajal, Phys. B **192**, 55 (1993).

[28] P. Giannozzi, O. Andreussi, T. Brumme, O. Bunau, M. Buongiorno Nardelli, M. Calandra, R. Car, C. Cavazzoni, D. Ceresoli, M. Cococcioni, N. Colonna, I. Carnimeo, A. Dal Corso, S. de Gironcoli, P. Delugas, R. A. DiStasio, A. Ferretti, A. Floris, G. Fratesi, G. Fugallo, R. Gebauer, U. Gerstmann, F. Giustino, T. Gorni, J. Jia, M. Kawamura, H.-Y. Ko, A. Kokalj, E. Küçükbenli, M. Lazzeri, M. Marsili, N. Marzari, F. Mauri, N. L. Nguyen, H.-V. Nguyen, A. Otero-de-la-Roza, L. Paulatto, S. Poncé, D. Rocca, R. Sabatini, B. Santra, M. Schlipf, A. P. Seitsonen, A. Smogunov, I. Timrov, T. Thonhauser, P. Umari, N. Vast, X. Wu, and S. Baroni, J. Phys.: Condens. Matter **29**, 465901 (2017).

[29] P. Giannozzi, S. Baroni, N. Bonini, M. Calandra, R. Car, C. Cavazzoni, D. Ceresoli, G. L. Chiarotti, M. Cococcioni, I. Dabo, A. Dal Corso, S. de Gironcoli, S. Fabris, G. Fratesi, R. Gebauer, U. Gerstmann, C. Gougoussis, A. Kokalj, M. Lazzeri, L. Martin-Samos, N. Marzari, F. Mauri, R. Mazzarello, S. Paolini, A. Pasquarello, L. Paulatto, C. Sbraccia, S. Scandolo, G. Sclauzero, A. P. Seitsonen, A. Smogunov, P. Umari, and R. M. Wentzcovitch, J. Phys.: Condens. Matter **21**, 395502 (2009).

[30] J. P. Perdew and Y. Wang, Phys. Rev. B **33**, 8800 (1986).

[31] J. P. Perdew, K. Burke, and M. Ernzerhof, Phys. Rev. Lett. **77**, 3865 (1996).

[32] H. J. Monkhorst and J. D. Pack, Phys. Rev. B **13**, 5188 (1976).

[33] R. F. W. Bader, Chem. Rev. **91**, 893 (1991).

[34] R. A. P. Ribeiro, S. R. De Lazaro, and S. A. Pianaro, J. Magn. Magn. Mater. **391**, 166 (2015).

[35] A. Chartier, P. D'Arco, R. Dovesi, and V. R. Saunders, Phys. Rev. B **60**, 14042 (1999).

[36] R. Tackett, G. Lawes, B. C. Melot, M. Grossman, E. S. Toberer, and R. Seshadri, Phys. Rev. B **76**, 024409 (2007).

[37] Y. Moritomo, Y. Ohishi, A. Kuriki, E. Nishibori, M. Takata, and M. Sakata, J. Phys. Soc. Jpn. **72**, 765 (2003).

[38] G. B. Jensen and O. V. Nielsen, J. Phys. C **7**, 409 (1974).

[39] See Supplemental Material at http://link.aps.org/supplemental/10.1103/PhysRevB.105.094430 for the experimental and calculated structural data of Mn_3O_4 at selected temperatures and pressures.

[40] S. Hirai, Y. Goto, Y. Sakai, A. Wakatsuki, Y. Kamihara, and M. Matoba, J. Phys. Soc. Jpn. **84**, 114702 (2015).

[41] H. Chang, I.-Y. Hwang, J.-H. Chung, J. R. Stewart, W. Higemoto, and Y. Miyake, Phys. Rev. B **97**, 014406 (2018).

[42] T. Byrum, S. L. Gleason, A. Thaler, G. J. MacDougall, and S. L. Cooper, Phys. Rev. B **93**, 184418 (2016).

[43] L. I. Mirkin, *Handbook of X-Ray Analysis of Polycrystalline Materials* (Springer, New York, 1964).

[44] N. O. Golosova, D. P. Kozlenko, S. E. Kichanov, E. V. Lukin, H. P. Liermann, K. V. Glazyrin, and B. N. Savenko, J. Alloys Compd. **722**, 593 (2017).

[45] D. P. Kozlenko, N. M. Belozerova, S. S. Ata-Allah, S. E. Kichanov, M. Yehia, A. Hashhash, E. V. Lukin, and B. N. Savenko, J. Magn. Magn. Mater. **449**, 44 (2018).

[46] S. Zouari, L. Ranno, A. Cheikh-Rouhou, O. Isnard, M. Pernet, P. Wolfers, and P. Strobel, J. Alloys Compd. **353**, 5 (2003).

[47] S. Hirai, A. M. dos Santos, M. C. Shapiro, J. J. Molaison, N. Pradhan, M. Guthrie, C. A. Tulk, I. R. Fisher, and W. L. Mao, Phys. Rev. B **87**, 014417 (2013).

[48] I. Efthimiopoulos, Z. T. Y. Liu, S. V. Khare, P. Sarin, T. Lochbiler, V. Tsurkan, A. Loidl, D.

Popov, and Y. Wang, Phys. Rev. B **92**, 064108 (2015).

[49] D. Das and S. Ghosh, J. Phys. D **48**, 425001 (2015).

[50] P. Gopal, R. De Gennaro, M. S. D. S. Gusmao, R. Al Rahal Al Orabi, H. Wang, S. Curtarolo, M. Fornari, and M. Buongiorno Nardelli, J. Phys.: Condens. Matter **29**, 444003 (2017).

[51] C. Franchini, R. Podloucky, J. Paier, M. Marsman, and G. Kresse, Phys. Rev. B **75**, 195128 (2007).

[52] P. R. Garcês Gonçalves, H. A. De Abreu, and H. A. Duarte, J. Phys. Chem. C **122**, 20841 (2018).

[53] F. Birch, J. Geophys. Res. **91**, 4949 (1986).

[54] K. Zhao, Y. Wang, Y. Sui, C. Xin, X. Wang, Y. Wang, Z. Liu, and B. Li, Phys. Status Solidi - Rapid Res. Lett. **9**, 379 (2015).

[55] K. K. Pandey, H. K. Poswal, R. Kumar, and S. M. Sharma, J. Phys.: Condens. Matter **25**, 325401 (2013).

[56] J. Zhao, L. Xu, Y. Liu, Z. Yu, C. Li, Y. Wang, and Z. Liu, J. Phys. Chem. C **119**, 27657 (2015).